Thin crystalline macroporous silicon solar cells with ion implanted emitter

Marco Ernst[a,*], Henning Schulte-Huxel[a], Raphael Niepelt[a], Sarah Kajari-Schröder[a], and Rolf Brendel[a,b]

[a]*Institute for Solar Energy Research Hamelin, D-31860 Emmerthal, Germany*
[b]*Department Solar Energy, Institute of Solid-State Physics, Leibniz Universität Hannover, D-30167 Hannover, Germany*

Abstract

We separate a (34 ± 2) µm-thick macroporous Si layer from an n-type Si wafer by means of electrochemical etching. The porosity is $p = (26.2 \pm 2.4)$ %. We use ion implantation to selectively dope the outer surfaces of the macroporous Si layer. No masking of the surface is required. The pores are open during the implantation process. We fabricate a macroporous Si solar cell with an implanted boron emitter at the front side and an implanted phosphorus region at the rear side. The short-circuit current density is 34.8 mA cm^{-2} and the open-circuit voltage is 562 mV. With a fill factor of 69.1 % the cell achieves an energy-conversion efficiency of 13.5 %.

1. Introduction

For cost saving reasons, the reduction of silicon consumption and, thus, wafer thickness and kerf losses is one of the current research goals in crystalline silicon photovoltaics [1]. Using macroporous silicon (MacPSi) is one of several options for the fabrication of thin crystalline silicon absorber layers without kerf loss [2], [3]. In this approach, the macroporous silicon layer is directly used as the absorber of the thin-film solar cell. The macroporous structure guarantees a low surface reflectance and an efficient light trapping. However, one challenge is the surface selective doping of the macroporous Si layers despite the through-going pores.

---

* Corresponding author. Tel.: +49-5151-999-644; fax: +49-5151-999-400.
E-mail address: ernst@isfh.de.

We recently reported on two different types of junction formation using macroporous silicon as the absorber of the solar cell [4], [5]. The first working solar cell from a detached MacPSi layer uses a heterojunction device process and achieved an energy-conversion efficiency of 7.2 % [4]. The second approach uses the growth of a p^+-type layer by epitaxy onto the n-type MacPSi layer for junction formation [5]. The epitaxial layer covers the full outer and inner surface of the macroporous layer and improves the energy-conversion efficiency to 13.1 % with a remarkable high short-circuit current density of 37.1 mA cm^{-2} for a (35 ± 2) μm-thick macroporous silicon solar cell.

In this paper we use ion implantation to selectively dope the outer surfaces of the macroporous silicon layer. We control the depth of implantation in the pores by the incident angle of implantation. Thus, no complex steps for side-selective doping are required. We term macroporous silicon solar cells with ion implanted emitter "MacImplant" cells.

2. Implantation in macroporous silicon

2.1. Sample preparation

Figures 1a to 1d sketch the macroporous silicon process. The process starts with an (100)-oriented, Czochralski-grown, shiny-etched, 6-inch, n-type Si substrate wafer with a thickness of (305 ± 20) μm. The substrate resistivity is (1.5 ± 0.2) Ωcm. The front side of the wafer is photolithographically patterned with hexagonally arranged inverted pyramids with a distance of $2r_0 = 8.0$ μm of the pyramids tips. A highly phosphorus doped region with a sheet resistance of 10 Ω at the rear side provides an ohmic contact during electrochemical etching.

The etching procedure of the macroporous absorber and separation layer (Figs. 1b and 1c) is performed under rear side illumination [6] in a 3 wt% aqueous hydrofluoric acid (HF) with 7.5 vol% acetic acid at 20 °C. The etching procedure is described elsewhere [7]. The etched circular area is 133 cm^2. The separation layer has a porosity of 100 %. The macroporous absorber layer is attached to the substrate only at the unetched rim of the substrate wafer [7].

For the further processing steps, the macroporous absorber layer is detached from the substrate (Fig. 1d). The side that was facing the substrate prior to detachment becomes the front side of the solar cell.

We then reduce the area of the macroporous Si layer to 6 cm × 6 cm in preparation for ion implantation. The implantation process is sketched in Figures 2a and 2b. In order to avoid an entire implantation of the inner pore surface, the ion beam is inclined with an angle of 25° to the surface normal. With the measured pore diameter, the implanted regions should reach approximately 9 μm deep into the
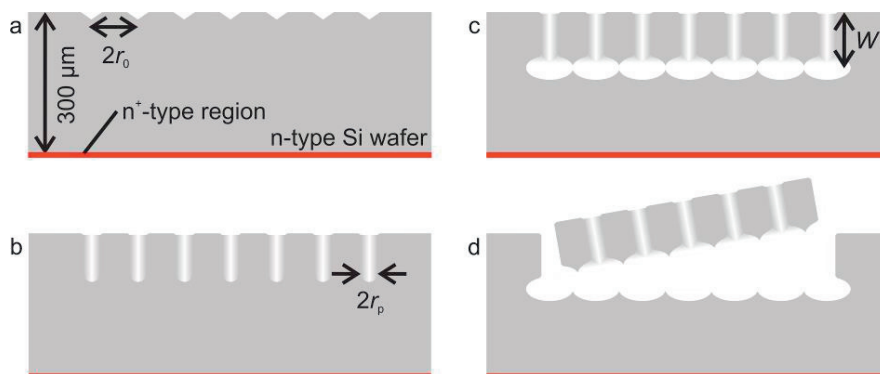

Fig. 1. Illustration of the macroporous silicon process (a) starting with a pre-structured n-type Si wafer, (b) and (c) macroporous absorber and separation layer formation, (d) detachment of the macroporous layer.
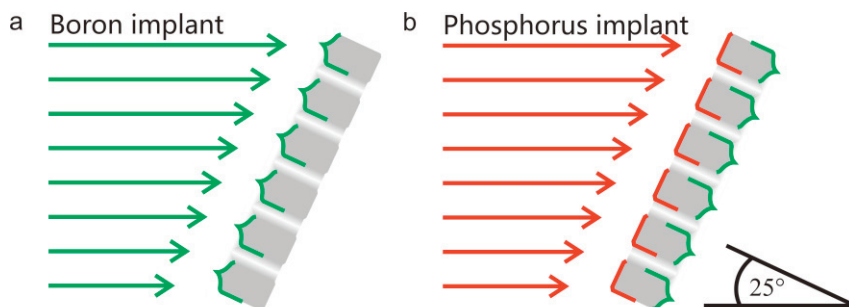
Fig. 2. Illustration of the implantation of (a) the boron emitter at the front side, and (b) the phosphorus region at the rear side under an angle of 25° to the surface normal.

pores. The ion implantation process allows for selectively doping the outer surfaces of macroporous Si layers without necessitating for complex masking steps. Second, the emitter is also present at the pore walls. This improves the carrier collection.

First, we perform an RCA cleaning [8] and implant boron atoms into the front side of the macroporous layer with an acceleration energy of 20 keV and a dose of 1.5×10^{15} cm^{-2}. Then implantation of phosphorus into the rear side of the layer is performed with an acceleration energy of 20 keV and a dose of 2.0×10^{15} cm^{-2}. We anneal the samples at temperatures ≥ 1000 °C for dopant activation and diffusion. Afterwards the macroporous layers are cut by a laser into 25 mm × 25 mm-sized pieces.

2.2. Structural analysis

Figure 3a shows a cross-sectional scanning electron microscope (SEM, S-4800 from Hitachi) micrograph of a $W = (34 \pm 2)$ µm-thick MacImplant solar cell. Electrochemical etching of the separation layer creates a surface texture at the front side. The pore diameter is $2r_\mathrm{p} = (4.3 \pm 0.2)$ µm. Thus, the porosity is $p = (26.2 \pm 2.4)$ %. The dashed box in Fig 3a marks the region where we determine the position of the pn-junction using electron beam induced current (EBIC) technique.

Figure 3b shows an SEM micrograph of the front side overlaid by the EBIC-signal (red). In contrast to our expectations, we observe a pn-junction at both sides of the pores. We find the same result in cross-sections taken in a plane perpendicular to the SEM micrograph shown here. The measured depth of the B-implantation at the pore walls ranges from 12 µm to 16 µm.
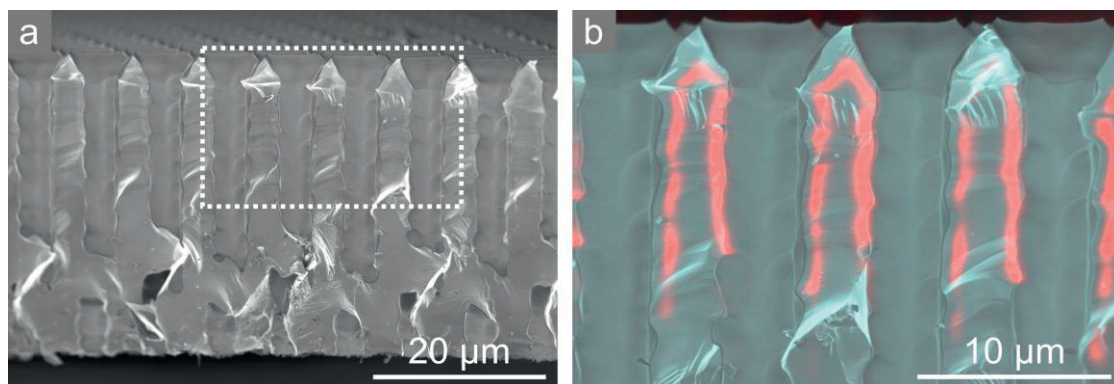

Fig. 3. (a) Cross-sectional SEM micrograph of a (34 ± 2) µm-thick MacImplant solar cell. (b) Detailed EBIC (red) and SEM micrograph of the pn-junction at the front side.
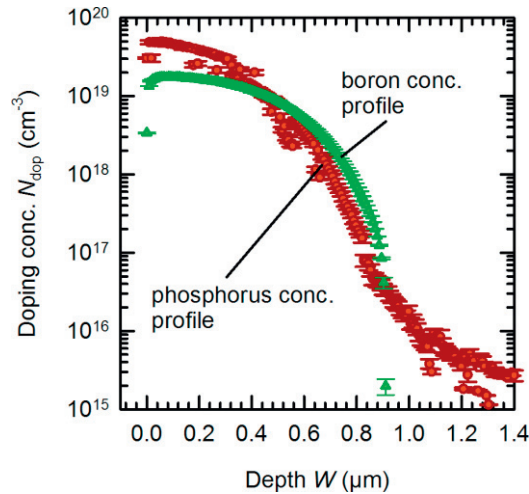
Fig. 4. Doping concentration profile of the boron- (green triangles) and phosphorus-implanted (red circles) region measured after annealing on planar reference samples.

2.3. Doping profile

We measure the doping concentration by electrochemical capacitance voltage profiling (CVP21 profile from WEP) on planar reference samples that received the same implantation and annealing procedure. Figure 4 shows the concentration profiles of the boron-implanted emitter (green triangles) and the phosphorus-implanted region (red circles). The peak concentration is 2×10^{19} cm^{-3} for the boron-implanted region and 5×10^{19} cm^{-3} for the phosphorus-implanted region. The depth of the boron- and phosphorus-profile is 0.9 µm and 1.0 µm, respectively.

The sheet resistance is measured by a 4-point probe measurement and is (36 ± 2) Ω for the boron emitter and (45 ± 2) Ω for the phosphorus doped region.

3. MacImplant solar cell

3.1. Solar cell preparation

Figure 5 sketches the solar cell. The boron emitter is at the front side and at the upper section of the pore walls. The phosphorus doped region is at the rear side and at the other side of the pore walls.

Directly after laser-cutting into 25×25 mm^2-sized samples, the macroporous Si layers are RCA-cleaned and the oxide layer from the previous annealing step is removed in a 5 wt% HF-solution.

We first selectively passivate the pore wall surfaces with a thermally grown oxide layer. Therefore we deposit a 70 nm thick SiN$_x$ film with a refractive index of 1.9 onto the front and rear side of the sample by means of plasma-enhanced chemical vapour deposition. Due to a low process pressure of 0.2 mbar, the SiN$_x$ film grows primarily on the outer surface but hardly in the pores. After an RCA cleaning procedure, an 80 nm thick oxide layer is grown in a wet thermal oxidization at 900 °C. Then, the SiN$_x$ film is selectively removed in 85 wt% ortho-phosphoric acid at 140 °C.

An RCA cleaning is followed by two cycles of plasma-assisted atomic layer deposition of Al$_2$O$_3$ to generate a thin tunnelling layer on the front side. One ALD cycle is equivalent to 0.12 nm aluminium oxide [9]. This layer prohibits a diffusion of the front contact aluminium through the p$^+$-type emitter.

The Al front side fingers are evaporated through a shadow mask with an angle of 55° to the surface normal to avoid penetration of Al into the pores. The spacing between the fingers is 2 mm and the width
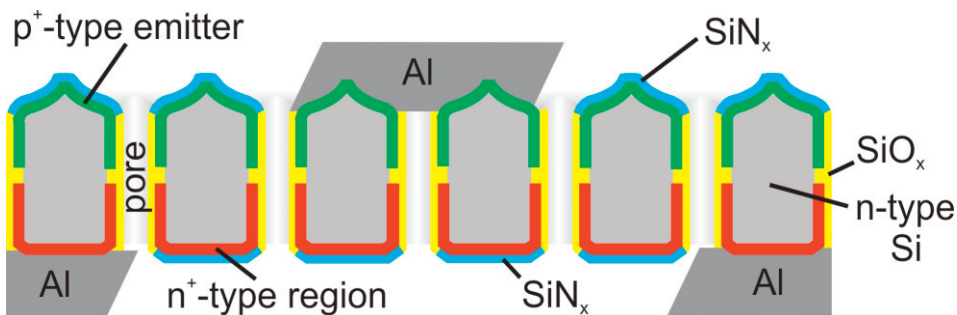
Fig. 5. Schematics of the macroporous solar cell (not to scale). A p+-type implanted emitter (green) is at the front side. An n+-type implanted region (red) is at the rear side. A SiNx layer (blue) is at the front- and at the rear side and a SiOx layer (yellow) is at the pore walls.

of the Al fingers is 110 µm. The rear-side grid is evaporated at interdigitated positions relative to the front-side grid (see Fig. 5) with an angle of 55° to the surface normal.

Then, a SiNx double layer is deposited for front surface passivation and as anti-reflection coating. The double layer consists of a 10 nm layer with a refractive index of 2.4 and a 100 nm layer with a refractive index of 2.05 as measured on planar reference samples. An identical SiNx layer stack is deposited onto the rear side of the samples. The interface is improved by annealing the samples in air on a hot plate at 350 °C for 2 min.

The active cell area of the MacImplant solar cell is reduced by laser-cutting to 3.92 cm^2 in order to remove the edges that suffered from handling. Then, the thin MacImplant solar cells are laser-bonded to an Al coated glass carrier to provide a good electrical contact and mechanical stability for device characterization. This so called AMELI-process is described elsewhere [10]. Aligning of the 38 µm-sized laser-welding spots to the centre of the 110 µm-wide Al fingers is enabled by the openings of the Al coating on the glass. Finally, the samples are annealed in air on a hot plate at 425 °C for 3 min. Figure 6a shows the front side of a MacImplant solar cell bonded to a glass carrier. The Al coating on the glass has a width of 13 mm. Figure 6b shows the rear side of the interconnected cell. The red dots illustrate the positions of the laser-welding spots.

We process planar, non-porous reference samples from an identical substrate wafer along with the MacImplant samples. The non-textured reference samples receive the p+-type implantation at the front side and the n+-type implantation at the rear side and are also bonded to a glass carrier.
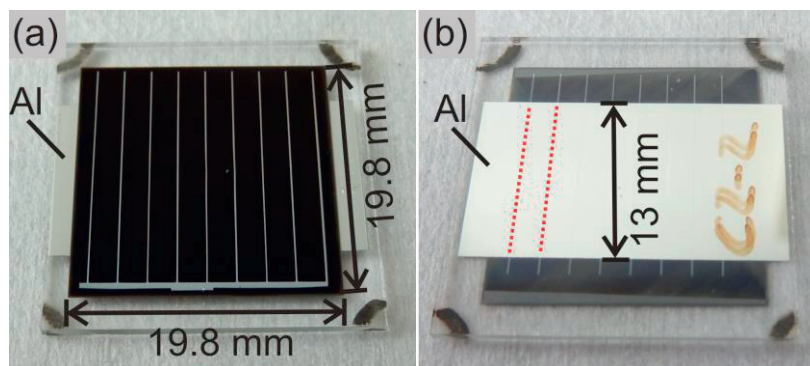

Fig. 6. MacImplant cell bonded to an Al coated glass carrier. (a) Front side of the solar cell. (b) Rear side of the cell. The red dots illustrate the positions of the laser-welding spots.
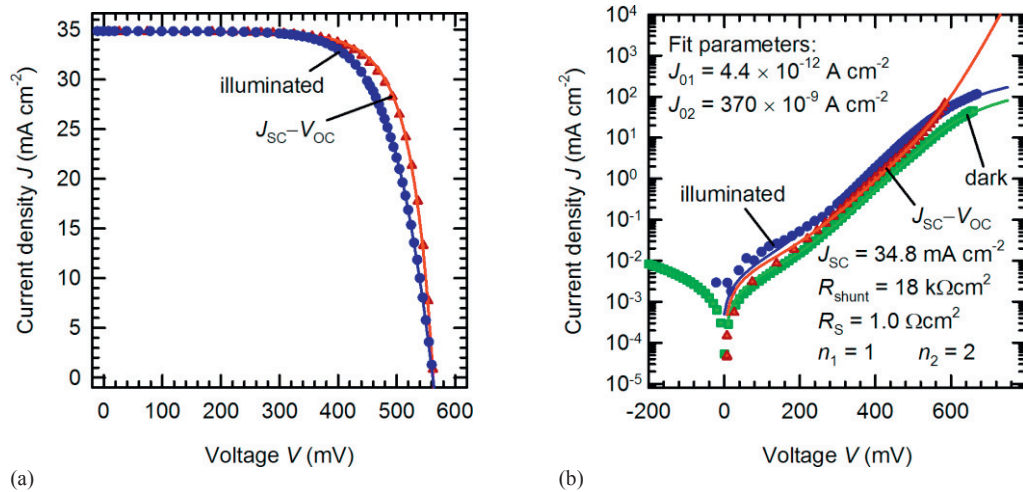
Fig. 7. (a) In-house measured illuminated *J–V* curve (blue circles) and J_{SC}–V_{OC} curve (red triangles) of the best MacImplant solar cell. The solid blue and red lines are fits from a two-diode model for the parameters shown in Fig. 7b. (b) Semilogarithmic plot of the illuminated *J–V* curve (blue circles), dark *J–V* curve (green boxes), and J_{SC}–V_{OC} curve (red triangles) of the best MacImplant solar cell. The solid blue, green and red lines are fits from a two-diode model for the parameters given in the figure.

3.2. Cell results

We measure the illuminated *J–V* curves at 25 °C under illumination by halogen lamps in a home built cell tester. The lamp to cell distance is adjusted to reproduce the short-circuit current density of a cell that was calibrated at Fraunhofer ISE CalLab under 1000 W m^{-2} of AM1.5G-illumination. We also measure the external quantum efficiency under one sun bias light and apply a spectral mismatch correction [11].

Figure 7a shows the *J–V* curve of the best out of three MacImplant solar cells. The best cell achieves an open-circuit voltage of 562 mV and a short-circuit current density of 34.8 mA cm^{-2} when measured with an A = 2.25 cm^2-sized aperture. With a fill factor *FF* = 69.1 % the cell achieves an energy-conversion efficiency of η = 13.5 %.

Table 1 lists the measured parameters for the MacImplant cells and planar reference cells. The lumped parallel resistance R_{shunt} = 18 kΩcm^2 of the best MacImplant cell is determined from the dark *J–V* curve at –0.5 V by Ohm's law. We determine the lumped series resistance R_S = 1.0 Ωcm^2 with the fill-factor method [12].

We fit the dark and illuminated *J–V* curves and the J_{SC}–V_{OC} characteristics with a two-diode model [13] with the voltage independent ideality factors 1 and 2. Figure 7b shows a semilogarithmic plot of the dark and illuminated *J–V* curves (green boxes and blue circles) and the J_{SC}–V_{OC} curve (red triangles).

Table 1. Electrical solar cell parameters

Cell	A (cm^2)	η (%)	*FF* (%)	*pFF* (%)	V_{OC} (mV)	J_{SC} (mA cm^{-2})
Best	2.25	13.5	69.1	73.7	562	34.8
Mean[a]	2.25	13.0 ± 0.5	68.8 ± 1.8	73.9 ± 0.5	550 ± 25	34.4 ± 0.5
Planar ref. mean[a]	4.25	15.0 ± 0.0	77.5 ± 0.1	79.9 ± 0.1	624 ± 1	31.2 ± 0.1

Aperture area A, energy-conversion efficiency η, fill factor *FF*, open-circuit voltage V_{OC}, and short-circuit current density J_{SC} of the illuminated *J–V* curves under one sun illumination at 25 °C. Pseudo fill factor *pFF* from J_{SC}–V_{OC} measurements.
[a]Average cell parameters of three processed solar cells.

For the fits (solid lines in the graph), we use the previously determined values of $R_{shunt} = 18$ kΩcm^2, $R_S = 1.0$ Ωcm^2, and $J_{SC} = 34.8$ mA cm^{-2}. The only fitted parameters are $J_{01} = 4.4 \times 10^{-12}$ A cm^{-2} and $J_{02} = 370 \times 10^{-9}$ A cm^{-2}.

4. Discussion

We observe a boron implanted region on both sides of the pores in Fig. 3b. We suggest that reflection of boron ions at the pore walls causes this effect. The ions are impinging under an angle of 65° with respect to the surface normal of the pore walls.

We use Iradina 1.0.4 to calculate the fraction of backscattered ions as a function of the angle of incidence of the ion beam [14]. Figure 8 shows the fraction of the backscattered ions for the boron ions (green triangles) and phosphorus ions (red circles) as a function of the angle of incidence. The fraction of the backscattered ions is lower for the phosphorus ions due to their higher atomic mass. The simulations show that 20.4 % of the boron ions and 14.5 % of the phosphorus ions are reflected at a planar silicon surface under an angle of incidence of 65° and an acceleration energy of 20 keV.

Iradina allows the simulation of ion beam irradiation on three-dimensional targets [14]. In order to understand the reflection in the pore walls we set up a three-dimensional target with a macropore. Figure 9 shows this geometry. The pore diameter is $2r_p = 4.3$ µm and the thickness of the unit cell is $W = 30$ µm. The ion beam enters the yz-plane with an inclination angle of 25° to the surface normal. The position of the ion beam is randomly distributed over this plane.

In order to illustrate the distribution of the implanted ions in the pore wall, the Cartesian coordinate system is transformed into the cylindrical coordinate system with radius r and polar angle φ. We then integrate the implanted ions over circular sectors with an angle $\Delta\varphi = 10°$ as a function of the pore depth x. The red region in Fig. 9 illustrates such a circular sector.

Figure 10 shows the implanted ions as a function of the polar angle φ and the pore depth x. The red area in the upper center is the region where the ion beam directly hits the pore wall. This region reaches approximately 9 µm deep into the pores. The orange and green areas at the shady side are the regions where the ion beam hits the pore wall mainly from the first reflection and reaches approximately 18 µm deep into the pores. Few ions experience more than one reflection and cause a weak implantation in the blue regions.
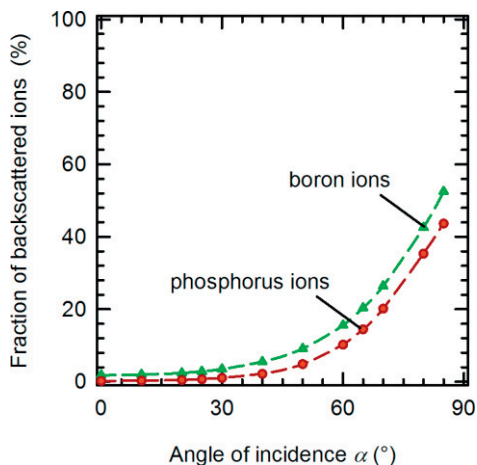

Fig. 8. Fraction of backscattered ions as a function of the angle of incidence α of the ion beam for boron (green triangles) and phosphorus (red circles). The dashed lines are to guide the eye.
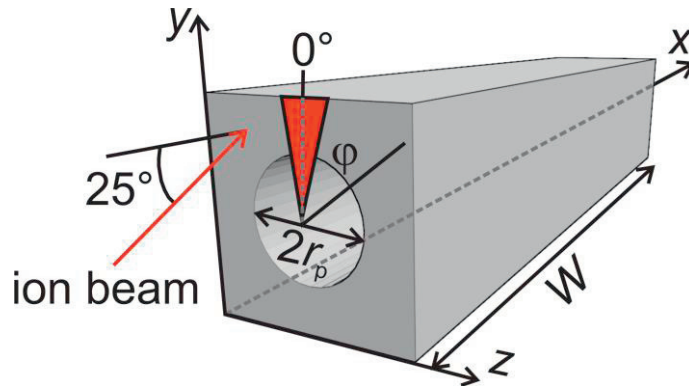
Fig. 9. Illustration of the three-dimensional pore geometry in Iradinia. The ion beam has an inclination angle of 25° to the surface normal.
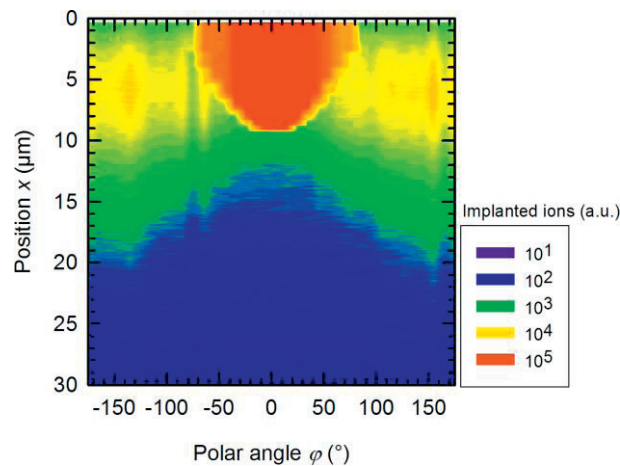

Fig. 10. Implanted ions as a function of polar angle φ and pore depth x.

We derive a local ideality factor n in the range of 1.5 to 2.5 from the slope of the dark J–V and J_{SC}−V_{OC} curves in the voltage range from 100 mV to 550 mV. At the maximum power point, the ideality factor is $n = 2$. We speculate that the MacImplant solar cells suffer from the overlapping B- and P-implanted regions in the center region of the pores, due to the unexpectedly deep implantation in the pore walls. However, the planar reference cells, which do not have these overlapping regions, show also high recombination losses. These losses are possibly caused by a poor SiN_x surface passivation and, thus, also degrade the performance of the MacImplant solar cells.

5. Conclusion

In this paper we have presented ion implantation into a macroporous silicon substrate for thin crystalline solar cells. In order to selectively dope the outer surfaces of the layer, we perform the implantation under an angle of incidence of 25° to the surface normal. Due to the inclined implantation angle a significant fraction of the ions is reflected at the pore walls and thus causes an implantation also in the shady side of the pore.

We developed proof-of-principle solar cells with implanted emitter and base contact regions. The depth of the emitter region at the pore walls leads to an excellent carrier collection that enables a short-

circuit current density of J_{SC} = 34.8 mA cm^{-2} for the only (34 ± 2) μm-thick device. The energy-conversion efficiency is 13.5 % when measured with a 2.25 cm^2-sized aperture mask.

Future development of the MacImplant solar cells requires optimization of the implantation depth at the pore walls and investigation of the recombination losses.

Acknowledgements

References

[1] ITRPV 2012, International Technology Roadmap for Photovoltaics Results 2012, Third Edition, Berlin 2012, www.ITRPV.net.

[2] Lehmann V, Hönlein W, Stengl R, Willer J, Wendt H. Verfahren zur Herstellung einer Solarzelle aus einer Substratscheibe, German patent DE4204455C1; Filing date: 29.01.1992.

[3] Brendel R, Ernst M. Macroporous Si as an absorber for thin-film solar cells. *Phys. Status Solidi RRL* 2010;**4**(1-2):40–2.

[4] Ernst M, Brendel R, Ferré R, Harder N. Thin macroporous silicon heterojunction solar cells. *Phys. Status Solidi RRL* 2012;**6**(5):187–9.

[5] Ernst M, Brendel R. Macroporous Silicon Solar Cells With an Epitaxial Emitter. *IEEE J. Photovoltaics* 2013;**3**(2):723–9.

[6] Lehmann V, Föll H. Formation Mechanism and Properties of Electrochemically Etched Trenches in n-Type Silicon. *J. Electrochem. Soc* 1990;**137**(2):653–9.

[7] Ernst M, Brendel R. Large area macroporous silicon layers for monocrystalline thin-film solar cells. In: *35th IEEE Photovoltaic Specialists Conference (PVSC)*: IEEE; 2010, p. 3122–3124.

[8] Kern W, Puotinen D. Cleaning solutions based on hydrogen peroxide for use in silicon semiconductor. *RCA Review* 1970;**31**:187–206.

[9] van Hemmen JL, Heil SBS, Klootwijk JH, Roozeboom F, Hodson CJ, van de Sanden MCM, et al. Plasma and Thermal ALD of Al2O3 in a Commercial 200 mm ALD Reactor. *J. Electrochem. Soc* 2007;**154**(7):G165-G169.

[10] Schulte-Huxel H, Bock R, Blankemeyer S, Merkle A, Brendel R. Aluminum-Based Mechanical and Electrical Laser Interconnection Process for Module Integration of Silicon Solar Cells. *IEEE J. Photovoltaics* 2012;**2**(1):16–21.

[11] King D, Hansen B. A sensitivity analysis of the spectral mismatch correction procedure using wavelength-dependent error sources (solar cell testing). In: *22nd IEEE Photovoltaic Specialists Conference (PVSC)*: IEEE; 1991, p. 459–465.

[12] Green MA. Solar Cells: Operating Principles, Technology and System Applications. Sydney, Australia: Univ. New South Wales; 1998; p. 96.

[13] Sah C, Noyce R, Shockley W. Carrier Generation and Recombination in P-N Junctions and P-N Junction Characteristics. *Proc. IRE* 1957;**45**(9):1228–43.

[14] Borschel C, Ronning C. Ion beam irradiation of nanostructures – A 3D Monte Carlo simulation code. *Nuclear Instruments and Methods in Physics Research Section B: Beam Interactions with Materials and Atoms* 2011;**269**(19):2133–8.